Article

Identification of Degradation Mechanisms in Slot-Die-Coated Nonfullerene ITO-Free Organic Solar Cells Using Different Illumination Spectra

Belén Arredondo,* Gonzalo del Pozo, Enrique Hernández-Balaguera, Diego Martín Martín, María del Carmen López González, Beatriz Romero, Eduardo López-Fraguas, Ricardo Vergaz, Xabier Quintana, Jani Lamminaho, Elodie Destouesse, Mehrad Ahmadpour, Vida Turkovic, and Morten Madsen

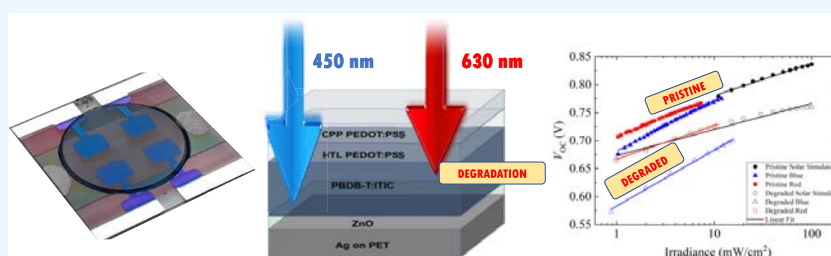Cite This: https://dx.doi.org/10.1021/acsaem.0c00711

Read Online

ACCESS | Metrics & More | Article Recommendations | Supporting Information

ABSTRACT: In this work, we have studied degradation mechanisms of nonfullerene-based organic solar cells with PET/Ag/ZnO/ PBDTB-T:ITIC/PEDOT:PSS/CPP PEDOT:PSS device structure. We compare pristine and degraded samples that were subjected to outdoor degradation following the standard ISOS-O2 protocol. The ideality factors for different incident wavelengths obtained from open-circuit voltage vs irradiation level and current density−voltage ($J−V$) measurements at different temperatures indicate that for aged samples recombination is governed by the Shockley−Red−Hall mechanism occurring in a region near the anode. Samples were also characterized using impedance spectroscopy and fitted to an electrical model. Impedance parameters were used to obtain mobility, indicating a clear degradation of the active layer blend for aged samples. The change in the chemical capacitance also reveals a worsening in carrier extraction. Finally, two-dimensional (2D) numerical simulations and fits to experimental $J−V$ curves confirm the existence of a layer near the anode contact with poorer mobility and a decrease in the anode work function for the degraded samples.

KEYWORDS: organic solar cells, degradation, nonfullerene, slot-die coating, ITO-free, flexible

INTRODUCTION

Most common organic solar cells (OSCs) are based on a solution-processed bulk heterojunction (BHJ) layer composed of a conjugated polymer as the donor and typically a fullerene derivative as the electron acceptor ($PC_{60}BM/PC_{70}BM$). To date, BHJ solar cells using fullerene acceptors have typically exhibited a power conversion efficiency (PCE) of around 5%[1] and rarely exceeding 10%,[2−4] mainly due to several fullerene-related drawbacks such as a difficulty in the tunability of the electronic molecular levels that limits the open-circuit voltage and limited light absorption. Likewise, extensive work has been carried out for understanding the degradation mechanisms of fullerene-based OSCs.[5−13]

In the past years, great efforts have been dedicated to synthesize new acceptors with easily tunable properties by chemical modification. In this context, nonfullerene acceptors have become widely popular because of their outstanding optical absorption, good electron transport mobility, easily adjustable optical band gap, low synthetic cost, and good miscibility with polymers.[14−20] Several studies reported fullerene-free devices with a boosted PCE of around 14−16% in single-junction solar cells.[18,21−24] The ease with which energy levels are tuned opens the possibility to optimize light harvesting in different spectral regions, synthesizing acceptors with absorption regions complementary to those of the donor material, and facilitates devices with open-circuit voltages above 1.1 V and low voltage losses.[25,26]

A
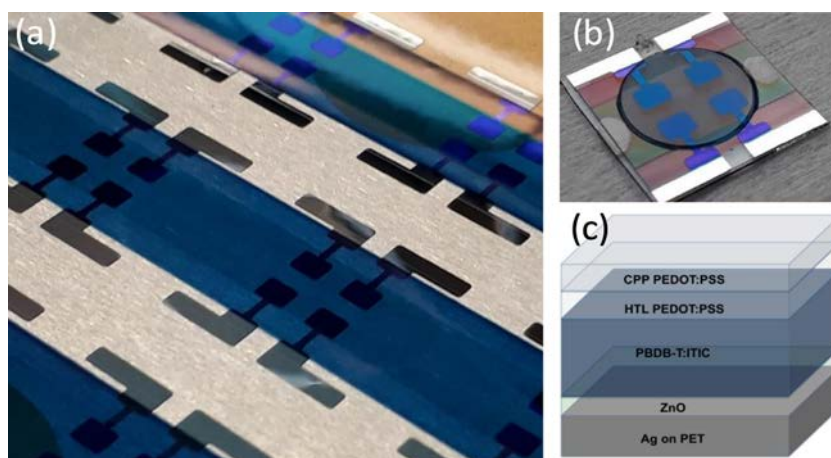
Figure 1. (a) Cell layout on a PET foil, (b) encapsulated sample, and (c) layer structure.

Nevertheless, to the best of our knowledge, not many studies have been carried out on the degradation and stability of fullerene-free solar cells. Few studies reveal that nonfullerene devices show good stability in air and under dark storage.[27,28] However, Doumon et al. performed a comparative study on the photostability of PBDB-T:ITIC vs a standard fullerene solar cell based on PBDB-T:PC$_{70}$BM.[29] These fullerene-free solar cells were first reported by Zhao et al. with PCE more than 11% using a combination of the conjugated polymer PBDTB-T poly[(2,6-(4,8-bis(5-(2-ethylhexyl)thiophen-2-yl)-benzo[1,2-b:4,5-b′]dithiophene))-alt-(5,5-(1′,3′-di-2-thienyl-5′,7′-bis(2-ethylhexyl)benzo[1′,2′-c:4′,5′-c′]dithiophene-4,8-dione))] as the donor and a small molecule ITIC (3,9-bis(2-methylene-(3-(1,1-dicyanomethylene)-indanone))-5,5,11,11-tetrakis(4-hexylphenyl)-dithieno[2,3-d:2′,3′-d′]-s-indaceno-[1,2b:5,6-b′] dithiophene) as the acceptor.[14] Doumon et al. concluded that although ITIC-based solar cells performed better in terms of initial PCE, they exhibited poorer photostability than PC$_{70}$BM-based devices due to lowered mobility upon light exposure for the investigated system. The same was observed by Upama et al., who assigned the PBDB-T:ITIC device degradation to the broadening of Urbach energy and a subsequent increase in the energetic disorder in the active layer, as well as the increased exponential distribution of localized states, which act as trap-mediated recombination centers.[15] Du et al. assigned this increase of energetic traps in ITIC-, ITIC-M-, and ITIC-DM-based systems to the breaking of conjugation and found that fluorination as well as avoidance of methyl groups of the end group stabilizes the molecules against photooxidation.[30] They also observed a reorientation of ITIC molecules in the blend from face-on to edge-on upon degradation, which further negatively affects the efficiency. Further importance of the molecular structure and conformation in the photostability of nonfullerene acceptor (NFA)-based systems in air was demonstrated by Luke et al., who observed less initial photoinduced conformational change induced by noncovalent interactions with environmental molecules in the case of the planar IDTBR, leading to a stronger photostability as opposed to amorphous nonplanar IDFBR.[31] Recently, a relation between the stability and the lowest unoccupied molecular orbital (LUMO) levels of the nonfullerene acceptors was reported, where the yield of the highly reactive radical superoxide anions is strongly enhanced in lower-lying LUMO NFAs, which negatively affects their photostability,

as the superoxide radical anion initiates the radical chain oxidation of the active layer.[19] Thus, these few initial studies on the stability of fullerene-free solar cells underline the NFA-specific, yet unrevealed, degradation mechanisms, which need to be further investigated and better understood to provide long lifetimes to these otherwise highly efficient devices.

In this work, we have studied the dominant recombination mechanisms and active layer transport properties occurring in a solar cell based on the polymer PBDTB-T, blended with the acceptor molecule ITIC on a polyethylene terephthalate substrate with structure PET/Ag/ZnO/PBDTB-T:ITIC/HTL PEDOT:PSS/CPP105D PEDOT:PSS. Current density−voltage (J−V) and impedance spectroscopy (IS) measurements with equivalent-circuit analysis and physical modeling are used to investigate the dynamical processes governing the device. Moreover, impedance spectra using two monochromatic illuminations (λ = 630 and 450 nm) and J−V curves for varying temperatures provide information about the mobility and activation energy of the dominant carrier recombination path. Finally, we have performed numerical device simulations using SILVACO ATLAS to support the conclusions obtained from the experiment.

■ EXPERIMENTAL METHODS

The organic photovoltaic (OPV) structure used in this study is presented in Figure 1c. A heat-stabilized PET foil with a thickness of 125 μm (Melinex ST504) from DuPont Teijin Films was used as a substrate. ZnO nanoparticles (H-SZ01034) were purchased from GenesInk and were in-line filtered with a 0.2 μm RC filter from Whatman. PBDB-T and ITIC were purchased from Brilliant Matters Inc. The active layer solution was prepared with a ratio 1:1 (PBDB-T:ITIC) at a total concentration of 30 mg/mL in chlorobenzene with 0.5% v/v 1.8-diiodooctane. The solution was stirred at 80 °C for 3 h in ambient conditions. PEDOT:PSS (both HTL solar and CPP105D) was purchased from Heraeus. Silver nanowires (10% v/v) in isopropanol were added to the CPP105D prior to deposition to increase the conductivity of the top electrode.

Organic solar cells were fabricated in the following inverted device configuration: PET/Ag/ZnO/PBDB-T:ITIC/HTL PEDOT:PSS/CP105D PEDOT:PSS. All devices were processed in ambient conditions, except for the vacuum-deposited bottom electrode. For silver deposition, the PET substrates were pretreated with DC argon plasma in vacuum.

Silver electrodes (around 100 nm) were deposited using DC magnetron sputter (power 150 W, pressure 6 × 10^{-3} mbar, time 170 s) through a shadow mask that defines the small-scale cell or module area. The whole process was done in a roll-to-roll (R2R) vacuum line.

Table 1. Slot-Die Coating Parameters and Layer Thicknesses

		fabrication details			
	pumping speed (mL/min)	coating speed (mm/s)	coating gap (μm)	thickness (nm)	annealing
ZnO	0.05	12	200	30	100 °C (10 min)
PBDB-T:ITIC	0.035	6.3	200	300	
PEDOT:PSS HTL	0.06	7	200	100	
PEDOT:PSS CPP105D	0.05	7	250	100	65 °C (5 min)
					60 °C (5 min)

Solution-based slot-die coatings were performed using a motorized film applicator (Erichsen COATMASTER 510), which was custom modified for slot-die coating. The coating system holds a vacuum plate containing a heating element, for combined substrate fixture and substrate heating. A syringe pump (Harvard Apparatus PHD 2000) was used for controlled ink delivery. During coating, the syringe can be heated in a custom-build aluminum sleeve with silicone heater pads. The slot-die head was custom-built from stainless steel, and the heating of the slot-die head was done with a heating cartridge. Shims and meniscus guides were used to limit coating widths to 11 mm with ETL and an active layer. In the case of PEDOT:PSS HTL and CPP105D, shim and meniscus guide were used to limit the coating width to 7 mm. The vacuum plate was heated to 70 °C before the coating process was started and kept at this temperature throughout the coating process. The slot-die coating steps were performed under ambient air. Used coating parameters with resulting film thicknesses can be seen in Table 1.

During the active layer coating process, both the slot-die head and the syringe were heated to 60 °C. The PEDOT:PSS HTL Solar solution was coated directly, following coating of the active layer. Annealing of the foils after ZnO and at the very end (the complete layer stack) was performed in a vacuum oven. PET foil dimensions were 350 mm × 100 mm containing 60 samples in four rows. Each sample contained four devices that had an active area of 5.4 mm^2. The cell layout on the PET foil is seen in Figure 1a, and more details on the development of the cells from scalable fabrication methods can be found in ref 32.

Finally, samples were cut from the foil and glued (Permabond 105) on a glass substrate, followed by encapsulation with a round glass cover. Delo KATIOBOND LP655 was used as encapsulation glue, which was cured under UV light. Encapsulated samples and layer structure can be seen in Figure 1b,c, respectively.

Spectral response characteristics (external quantum efficiency, EQE) were taken using a custom-made system based on a Xe lamp light source and a double grating monochromator. The system is equipped with a monitor cell to compensate for temporal fluctuations in the light source. Chopped light together with a lock-in amplifier was used to maximize the signal-to-noise ratio.

Electrical measurements were carried out using an AutoLab potentiostat/galvanostat model PGSTAT204 (Eco-Chemie), equipped with the FRA32M impedance module and the Metrohm AutoLab optical bench. The instrument was controlled by a computer and driven by the NOVA 2.1.4 software. Experimental $J-V$ characteristics were obtained by performing a cyclic voltammetry test from −0.3 to 1.2 V. Impedance spectroscopy (IS) measurements were carried out immediately after $J-V$ experiments, by configuring the AutoLab to apply sinusoidal signals of 50 mV amplitude from 1 MHz to 1 Hz under open-circuit conditions. Fitting of all of the impedance spectra was performed using Scribner's ZView software. Both techniques were performed for three illumination spectra (under white, blue, and red illuminations), varying illumination intensities from 1 up to 10 or 100 mW/cm^2 for blue and red or white, respectively, using a calibrated silicon photodiode. Under white illumination conditions, the photovoltaic cell performance was analyzed using a Newport VeraSol-2 light-emitting diode (LED) class AAA solar simulator calibrated with an NIST-certified KG3 filtered Si reference cell.

Outdoor lifetime testing was carried out according to the International Summit on OPV Stability (ISOS) standard O-2 protocol.[33] The degradation of the samples was carried out in two periods of the year with different environmental conditions. Therefore, a "dry" and a "wet" degradation can be distinguished. The wet degradation was performed over a period of 525 h (22 days) with 131.3 equivalent hours of sun, 59.13% average humidity (with 28.5 and 94.8% as the lowest and highest values, respectively), and −1.6/17.3 °C minimum/maximum temperature. It is worth noticing that the maximum humidity corresponds to rainy days, thus causing the samples to get wet. The dry degradation has been carried out over 216 h (9 days) with 86.6 equivalent hours of sun, 38.4% average humidity (between 15.5 and 71.3%), and 10.2/30.6 °C minimum/maximum temperature.

Furthermore, the open-circuit potential was measured at different temperatures (from 293 to 333 K) to analyze the temperature-dependent device characteristics. The measurements were performed by inserting the cells in a TS102GXY hot/cold stage by Instec, operated under 24 V (DC) and 5 A. A 100 W platinum RTD is its temperature sensor. The stage contains a PID-controlled mk2000 Peltier that allows an accurate temperature setting (±0.05 °C) in the range explored in this work. We used a water-cooling pump system to guarantee stage temperatures below room temperature. In this experiment, we irradiated our cell using a proprietary LED-based sun simulator called SUNBOX. It is a class AAA device that allows the characterization of devices of 2 cm × 2 cm, placed on a platform 5 cm under a 34-LED PCB, in which every spectral set of LEDs can be controlled separately.[34]

Finally, the characterization was performed on four samples, with four devices each, that is, a total of 16 nominally equal devices. All devices were characterized in the pristine state showing similar DC/AC electrical behavior. Statistical information (average values and standard deviation) of PCE, fill factor (FF), J_{SC}, and V_{OC} can be found in the Supporting Information.

■ RESULTS AND DISCUSSION

The inset in Figure 2a shows the energy-level schematic. The energy difference between the highest occupied molecular
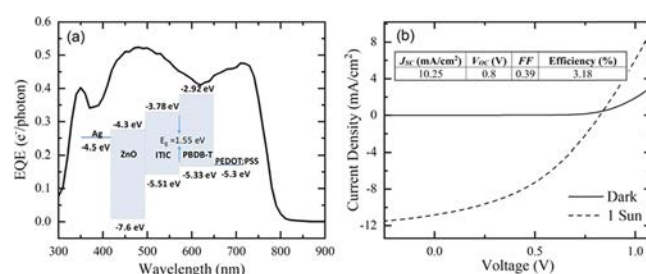
Figure 2. (a) External quantum efficiency (EQE). The inset shows the energy-level diagram. (b) $J-V$ characteristic in dark and under 1 sun illumination AM1.5 (100 mW/cm^2) of the pristine device.

orbital (HOMO) of PBDB-T and the LUMO of ITIC provides an effective band-gap energy for the blend of 1.55 eV. In addition, the reduced energy barrier between the HOMO levels of the donor and the acceptor reduces the energy losses in the generation of free carriers.

Previous studies show the complementary absorption spectra of the acceptor ITIC and the donor PBDTB-T,[14,35] enhancing the initial device performance with respect to fullerene-based cells. This is confirmed with our EQE measurement shown in Figure 2a, with the appearance of spectral response characteristic extended to 800 nm, compared to cells based on PBDTBT:PCBM with no quantum efficiency in that part of the spectrum.[36]

In a previous study, the cell performance evolves positively during an ISOS-D-1 study in which the cells were illuminated when measured.[32] We also note that illumination of active layer cells in nitrogen has shown to provide a minor positive evolution in performance during the initial illumination phase in a different study. Moreover, we note that the conductivity of ZnO can also be improved with exposure to UV light and thus power conversion efficiency also increases.[37] Thus, devices were pretreated with irradiation from a solar simulator for a short time (approximately 60 s) to ensure maximum performance (long illumination times could result in degradation of the active layer system). $J-V$ characteristics in the dark and under 1 sun illumination and the corresponding performance parameters are shown in Figure 2b. Fresh devices exhibit moderate efficiency compared to those in previous related studies with cells based on the same active layer blend but different layer structure.[14,29] Also, devices show modest efficiency when compared to those in previous studies with indium tin oxide (ITO)-free nonfullerene flexible OSCs with a different active layer.[38] At this point, we emphasize that cells presented in this work are developed under industrial conditions from scalable processes in air (S2S slot-die coating), using flexible substrates and ITO-free electrodes. Combined, the expected efficiency is thus also lower than typically reported for this active layer material system or for other ITO-free nonfullerene systems. To further explain the initial low performance of the cells, we show the atomic force microscopy (AFM) images of PCE12:ITIC films developed from spin-coating and slot-die coating (see Figure S1 of the Supporting Information). Further optimization of this cell configuration is demonstrated in ref 32. At this point, it is not the aim of this work to maximize the efficiency but to investigate the stability and degradation pathways of cells fabricated without using fullerene and ITO. It is worth pointing out that the below experiments using different excitation wavelengths were carried out for degraded samples when the efficiency had gone down to 0.4%. The full lifetime plot is shown in the Supporting Information.

According to Figure 3, the ideality factors (n) of the fresh and degraded samples under dry conditions are obtained from the slope of the logarithmic fit of the open-circuit voltage (V_{OC}) vs illumination intensity (irradiance) with different light spectra: red, blue, and white light illumination. Using different excitation wavelengths, we can obtain information about the penetration depth of the optical input inside the active layer. The absorption in the red part of the spectrum is much more intense than in the blue region,[14,32] and since EQE is around 0.5 for the blue and 0.42 for the red light (that is, only a 15% difference; see Figure 2a), it follows from the Beer–Lambert law that red light is absorbed near the anode contact, while blue light penetrates deeper in the layer. To support this thesis, we have performed simulations using Silvaco TCAD of transmissivity and absorptivity as a function of the active layer depth for blue (450 nm) and red (630 nm) monochromatic illuminations (see Figure S2 of the Supporting
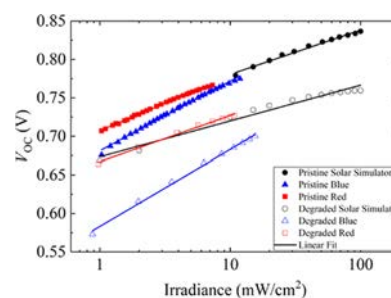
Figure 3. Open-circuit voltage (V_{OC}) vs light intensity for fresh and dry-degraded samples for white, red, and blue illumination. Ideality factor (n) is obtained from the slope, $-q/(nk_{B}T)$, of the linear regression.

Information). Our simulations validate our statement about the more intense absorption of red light near the anode contact. Thus, the value of the ideality factor, corresponding to the red- and blue-light illumination, is related to recombination mechanisms taking place in different spatial regions of the device. Moreover, the fact that open-circuit voltage tends to saturate with light intensity indicates the presence of nonselective contacts.[39] Note that this effect is more pronounced in the case of the degraded sample as shown in Figure 3. Ideality factors obtained from the fits are summarized in Table 2. The found values indicate a Shockley–Read–Hall

Table 2. Ideality Factors Obtained from the Fits Shown in Figure 3 for the Fresh and the Degraded Devices, Using Three Illumination Spectra; λ = 630 nm (Red), λ = 450 nm (Blue), and White Light

	n		
	red	blue	white
pristine	1.2	1.5	1
degraded	1	1.5	0.8

(SRH) recombination mechanism for red- and blue-light illumination in pristine samples (n values of 1.2 and 1.5, respectively). In contrast, n is around 1 for the aged devices under red-light illumination, while it remains unchanged for blue-light excitation. This indicates that the degradation is mostly affecting the space near the anode, where the red wavelength is being strongly absorbed. This result is in good agreement with that of Wang et al., who demonstrated that an interfacial reaction between the PEDOT:PSS hole transport layer and the ITIC acceptor was one of the main responsible mechanisms for nonfullerene organic solar cell (OSC) deterioration.[40] In an MIM (metal–intrinsic–metal) device or a p–i–n cell with low mobility and a homogeneous electric field across the device, an ideality factor of $n \approx 1$ indicates that the recombination near the contact dominates.[39] Numerical simulations are shown in the last section of the article, corroborating that these devices indeed behave as p–i–n cells. Hence, we can infer that, for the aged devices, recombination presumably takes place in an interfacial damaged layer (IDL) near the anode due to an increase of traps. The activation energy of these recombination centers will be analyzed later using temperature measurements. Furthermore, the diode ideality factor, before (fresh) and after degradation exposed to white light, follows those trends obtained with red wavelength excitation, indicating that recombination near the anode is the dominant mechanism even when illuminating with the whole

spectrum. This hypothesis is reinforced by the fact that, for the degraded diodes, V_{OC} under red and white illuminations overlaps, while for the blue light, open-circuit voltage is slightly higher. Note that the illumination intensity range covered by the red and blue colors cannot go beyond 10 mW/cm², corresponding to the maximum achieved by our LED setup.

Figure 4 shows the fill factor (FF) vs irradiance for pristine and degraded samples and for $\lambda = 630$ and 450 nm and white
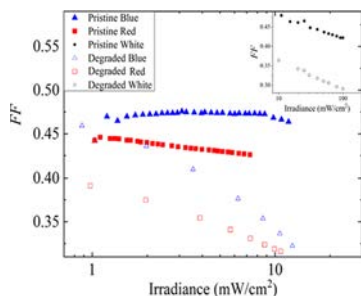
Figure 4. Fill factor (FF) vs irradiance for pristine and degraded samples illuminated with wavelengths of $\lambda = 630$ nm (red) and $\lambda = 450$ nm (blue). The inset shows FF values, for fresh and aged devices, at different illumination levels of white light.

illumination (the latter is shown in the inset). The origin of the FF, obtained from the $J-V$ curves, is determined by carrier extraction and carrier recombination, both competing processes governed by the mobility. As indicated in recent reports, there is optimized mobility at which efficiency and FF are maximum; for higher light intensities, carrier recombination increases, deteriorating the FF and power conversion efficiency.[41] In our study, FF values corresponding to blue illumination for the fresh cells remain almost unchanged with increasing irradiance. In contrast, when exposed to red light, the FF decreases slightly with light concentration. Degraded samples exhibit, as expected, a reduced FF that decays abruptly with light. Moreover, for white illumination, a similar behavior was identified to that obtained using the red wavelength excitation (refer to the inset of Figure 4). Later in the paper, we will discuss the influence on the FF of the mobility obtained from IS measurements.

Figure 5 shows representative examples of the experimental impedance spectra of the fresh (a) and degraded (b) samples at different color intensities measured at V_{OC}. Solid lines correspond to the fits using the equivalent electrical circuit of the inset (Matryoshka circuit). This circuital model has been widely used in previous studies[5,6] and consists of a series resistance R_S (associated with Ohmic losses at soldering and
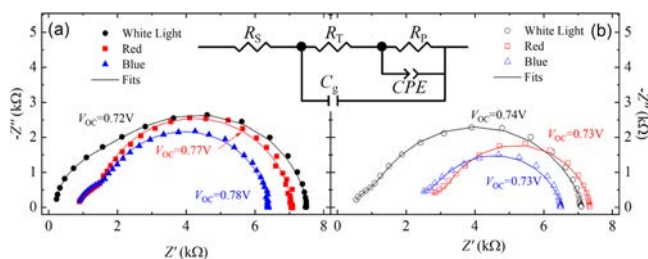
external wires), a recombination resistance R_P, a transport resistance R_T, a geometrical capacitance C_g, and a constant phase element (CPE) with impedance, $Z_{CPE}(j\omega) = 1/_{Q(j\omega)\alpha}$ connected as shown in the inset of Figure 5. Note that Q (with units of F × s$^{\alpha-1}$) and α (over the range 0−1) are the CPE's parameters, j is the imaginary unit, and ω is the angular frequency ($\omega = 2\pi f$; f where f is the frequency). Figure 5 exhibits an excellent agreement between the experimental and simulated data. The shape of the Cole−Cole curves is similar for the three illumination spectra used, for pristine and degraded samples, displaying (i) a capacitive loop at sufficiently high frequencies, related to carrier diffusion transport phenomena with a large active layer thickness ($L = 220$ nm) and (ii) a depressed semicircle in the low-frequency region, attributed to the recombination process, which involves a frequency dispersion of experimental impedance data. This CPE behavior that models a nonideal chemical capacitance leads to a time-constant distribution whose average characteristic value is $\tau_{lf} = (R_P Q)^{1/\alpha}$. Using this expression, an effective capacitance associated with the CPE can be found by matching the distributed time constant and that of the ideal RC time constant ($\tau_{lf} = R_P C_\mu$), yielding $C_\mu = R_P^{1-\alpha/\alpha} Q^{1/\alpha}$.[42] Importantly, a characteristic feature associated with the diffusion time can be obtained from the effective chemical capacitance: $\tau_d = R_T C_\mu$. Note that throughout this paper, τ_d provides valuable information on the device degradation associated with charge carrier mobilities.

Figure 6 shows the dependence of the impedance parameters on V_{OC} obtained from the fit of the circuital
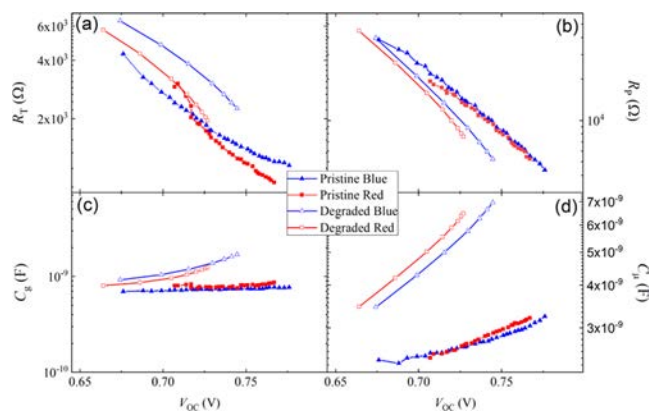
Figure 6. Evolution of parameters obtained from the impedance results using a Matryoshka circuit at open-circuit conditions for fresh and aged devices. (a) Transport resistance, R_T; (b) recombination resistance, R_P; (c) geometrical capacitance, C_g; and (d) effective chemical capacitance, C_μ (associated with a low-frequency R-CPE subcircuit).

Figure 5. Experimental impedance spectra, under open-circuit conditions, for white, red, and blue illuminations for (a) fresh and (b) degraded samples. Solid lines indicate the simulated results using the electrical equivalent circuit shown in the inset.

model to IS measurements under red and blue illuminations. Impedance parameters under white illumination for pristine and degraded devices cannot be compared since V_{OC} ranges do not overlap, as shown in Figure 3. Impedance parameters for red and blue illuminations in pristine and degraded samples are discussed below: (i) C_g remains almost constant ($C_g \approx 0.87$ nF) with open-circuit voltage for pristine devices, since its value is related to the geometrical capacitance of the active layer (refer to Figure 6c). Thus, the dielectric constant of the absorbing organic layer can be found from $C_g = \varepsilon\varepsilon_0 A/L$, resulting in $\varepsilon \approx 3.68$, where ε_0 is the permittivity of vacuum, A is the device area, and L is the active layer thickness. It is

noteworthy that the value of C_g slightly increases after degradation, particularly at high irradiation levels, which is typically attributed to device heating. Indeed, high illumination intensities must be applied after the degradation experiment to reach comparable open-circuit voltages. (ii) Both resistances, R_T and R_P, decrease with the radiation intensity, as expected (see Figure 6a,b, respectively). R_T increases with degradation for both colors, indicating that conduction is limited by the transport mechanisms. On the other hand, R_P decreases during the degradation process, indicating an increase of recombination, in particular for red illumination, which is in good agreement with the trend of the ideality factor for this color. (iii) Finally, it is important to point out that degradation significantly modifies the value of the effective chemical capacitance shown in Figure 6d (extracted from the CPE parameters; see above). This variation suggests an inefficient charge extraction. From a mathematical point of view, we can explain this using the dependence of C_μ value on Q and α parameters. Indeed, the value of C_μ depends critically on $Q^{1/\alpha}$, which increases upon degradation, reflecting a worsening of carrier extraction and a higher degree of disorder in the material (α value approximately decays from 0.9 down to 0.7, driving away C_μ from a purely capacitive behavior). This worsening in carrier extraction can also be related to a reduction of the anode work function, as will be discussed in the last section of the article.

For comparative purposes, the exponential dependence of R_P on V_{OC} shown in Figure 6b, with the characteristic slope $-q/(nk_BT)$, where T is the temperature and k_B is the Boltzmann constant, allows the calculation of the ideality factor. For fresh samples, n equals 1.6 (red) and 1.7 (blue), while for the aged devices, n is 1.2 (red) and 1.6 (blue). In effect, a close inspection of the n values reveals a high degree of similarity between the tendencies obtained for DC measurements (refer to Table 2) and those found using the IS technique.

The electron mobility at the open-circuit voltage can be estimated using $\mu = L^2/\tau_d V_T$, where V_T is the thermal voltage ($V_T = k_BT/q$). Table 3 shows the value of the mobilities

Table 3. Average Carrier Mobility Values Obtained for Fresh and Aged Samples Under 10 mW/cm² for Blue and Red Light and 100 mW/cm² for White Light

|	mobilities (cm²/(V s))		
	red	blue	white
pristine	6.2×10^{-3}	5.1×10^{-3}	1.9×10^{-2}
degraded	2.0×10^{-3}	1.6×10^{-3}	7.9×10^{-3}

obtained before and after degradation for all of the excitation wavelengths. Mobility for red and blue excitations exhibits a higher decrease than that obtained with white light illumination. Furthermore, mobilities in the pristine devices exhibit similar values for red and blue illuminations and thus the smaller FF for the red light shown in Figure 4 cannot be attributed to a change in mobility. This reduced FF and its decreasing trend with the irradiance for red light in the fresh sample can only be related to higher recombination for red wavelengths near the anode as indicated by the ideality factor. In the case of the degraded samples, the mobility decreases by a factor of 3 and therefore it governs the abrupt decrease of FF vs light intensity for all colors. This is a consequence of the increase in R_T for the degraded samples, suggesting that the

conduction is greatly limited by carrier transport after the aging process.

To gain further insight into the active layer degradation with time as the sample suffers the outdoor degradation protocol, the density of states (DOS) has been obtained from the chemical capacitance. Specifically, DOS has been calculated by fitting the chemical capacitance with eq 1, where N_n is the total density of states and E_L and σ_n are the center and width of the DOS, respectively.[43]

$$g_n(E - E_L) = \frac{N_n}{\sqrt{2\pi}\sigma_n}\exp\left[-\frac{(E_L - E)^2}{2\sigma_n^2}\right] \quad (1)$$

The fits of eq 1 to the experimental chemical capacitance shown in Figure 7a as solid lines indicate a broadening of the
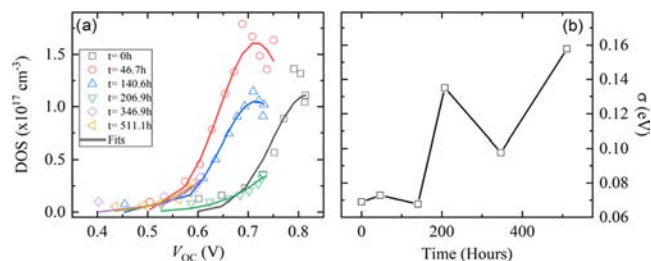
Figure 7. (a) Evolution of the Gaussian DOS parameters at the LUMO of ITIC obtained by fitting the chemical capacitance extracted from impedance at V_{OC} under different irradiances using eq 1. (b) Width of the DOS (σ) as a function of the degradation time, for the sample exposed to the outdoor degradation under high humidity levels.

DOS width with time under outdoor exposure. It is worth mentioning that the increase in the DOS width shown in Figure 7b corresponds to the days of measurement just after the first rainy days of the outdoor experiment. Although these DOS width values may present great uncertainty, the trend indicates an increasing degree of disorder in the active layer blend. This trend in σ_n is not observed when analyzing samples undergoing indoor degradation or samples undergoing outdoor degradation that were not exposed to rain (dry degradation, see the Supporting Information). This suggests that moisture is the main cause of the deterioration of the PBDTB-T:ITIC blend morphology.

Temperature-dependent $J-V$ measurements under white light at varying illumination levels in the pristine conditions are shown in Figure 8a. Linear decays (V_{OC} vs T), in all light-intensity experiments (from 20 up to 120 mW/cm², equivalent to 1.2 sun), can be observed. Open-circuit voltage as a function of temperature for all illumination levels was fitted to a linear regression. When the straight lines $V_{OC}-T$ are extrapolated toward the axis at $T = 0$ K, V_{OC} correlates with the activation energy E_a of the recombination process.[44] The values obtained for E_a have been represented as a function of the illumination level as shown in Figure 8b, where the activation energy decreases as the light intensity is increased. Comparing the obtained values of E_a with the donor−acceptor band gap E_g ($\approx$1.55 eV, see the inset of Figure 2a), smaller values of the activation energy are revealed ($E_a < E_g$), suggesting that the recombination mechanism is dominated by the mid-gap recombination centers.[44] Thus, this reinforces the thesis of SRH recombination phenomena in an IDL near the interface region as indicated by the n values obtained previously.
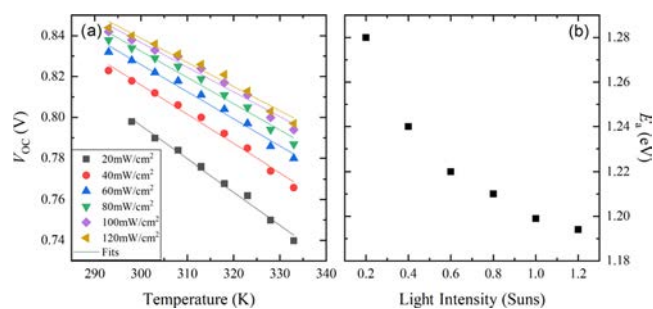
Figure 8. (a) Open-circuit voltage V_{OC} (extracted from current density−voltage curves) as a function of temperature under varying illumination conditions. (b) Activation energy E_a of the recombination process (obtained from the linear fit of V_{OC}−T characteristic) vs light intensity.

Moreover, the decreasing trend of E_a with light intensity shown in Figure 8b is related to the energy distribution of the trap-filling mechanism within the gap.

Finally, devices have been modeled using Silvaco ATLAS (see the Supporting Information for further details). Two-dimensional (2D) numerical simulations have been performed to consolidate our understanding of the dynamical mechanisms taking place inside the cells during degradation. Figure 9a
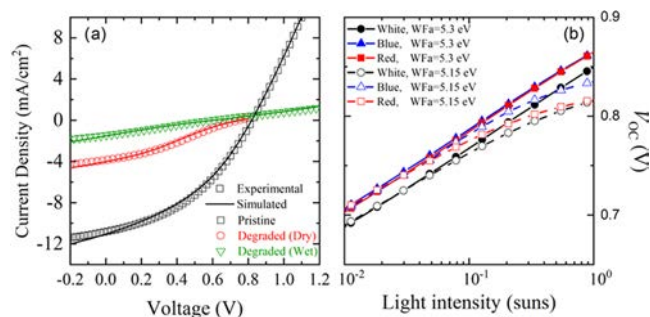
Figure 9. (a) Experimental (symbols) and numerically simulated (lines) J−V characteristics under 1 sun illumination AM1.5 (100 mW/cm^2) for the pristine and degraded devices. (b) V_{OC} vs light intensity obtained using white, blue, and red illuminations, with anode work functions of 5.3 and 5.15 eV, reproducing the effect of the anode degradation.

shows both experimental and simulated J−V characteristics under 1 sun illumination AM1.5 G for the pristine and degraded devices. For the pristine device, a majority carrier mobility of 8×10^{-3} (cm^2/(V s)) has been used to fit the experimental data, in close agreement with the values obtained from IS analysis. To fit the S-shaped J−V curves for the degraded devices, the ATLAS model has been modified to include a degradation of the anode contact (decrease of its absolute work function) together with a partial degradation of the front active layer blend (an ∼120 nm layer with reduced mobility near the anode contact) and an increased external series resistance. The parameter values leading to best fits are shown in Table 4. They confirm that degradation is caused both by the active layer and the anode contact worsening.

It should be emphasized that the good agreement between the experiment and the theory displayed in Figure 9a is achieved when both the anode work function (WF) is reduced and the decreased mobility of a layer is introduced in the physical model. Several attempts to fit the experimental data

Table 4. Parameters Used in the Simulations with Silvaco ATLAS for the Pristine and Degraded Devices

		damaged active layer		
	anode WF (eV)	series resistance (Ω)	mobility (cm^2/(V s))	depth (nm)
pristine	5.30	42	8×10^{-3}	
degraded (dry)	5.15	80	5×10^{-4}	120
degraded (wet)	5.00	300	4×10^{-4}	175

only by changing the anode WF or only by introducing a damaged layer did not lead to good fits.

As previously indicated, the ideality factor parameter can be obtained from the slope of the open-circuit potential (V_{OC}) vs light-intensity plot. Table 5 displays the n values extracted by

Table 5. Ideality Factors for the Fresh and the Degraded Cells Extracted from the Simulation Results Shown in Figure 9b Using a Theoretical Model of the Device Under Study for Red, Blue, and White Light Illuminations

	n		
	red	blue	white
pristine	1.3	1.3	1.2
degraded	1	1.2	0.9

simulating the evolution of V_{OC} with light intensity for two different anode WFs (see Figure 9b). These values agree with the trends of experimental n shown in Table 2. The ideality factors for red and white illuminations decrease toward $n \approx 1$, while it remains almost unchanged for the blue light. In summary, numerical simulations confirm that these devices behave as p−i−n cells with accumulation of majority carriers at the contacts, and the degradation emphasizes SRH recombination near the anode (with $n \sim 1$) as the dominant recombination mechanism.

These simulations agree well with experimental results and support the fact that degradation is caused by the combination of two mechanisms that are clearly observed when analyzing the electrical behavior using two distinct wavelengths. On the one hand, the change in the ideality factor shows a larger change for the red light when comparing fresh and degraded samples, indicating that the degradation is affecting the space near the anode, where the red wavelength is being strongly absorbed. On the other hand, the mobility of the blend is also decreasing for the degraded devices, and this is observed in a more pronounced change in the absolute value of V_{OC} for the blue light (see Figure 3) that penetrates deeper in the bulk.

■ CONCLUSIONS

In summary, an analysis of ideality factors using red and blue incident light reveals a greater change of n for longer wavelengths when fresh and aged samples are compared, suggesting that recombination is specifically taking place in a region near the anode, where the red light is mainly being absorbed. Blue light penetrates deeper in the sample, and no significant change in n is obtained. Moreover, temperature measurements reveal SRH recombination through intermediate trap states with an activation energy smaller that the optical band gap. IS parameters obtained from the fit to a standard equivalent circuit indicate an increase in the transport-limiting

mechanisms for the aged samples. This is also confirmed by the decrease in the mobility of the degraded devices obtained for all illumination spectra. The increase in the chemical capacitance for the degraded samples indicates an accumulation of carriers due to a worsening of carrier extraction. In addition, the width of the density of states in the LUMO obtained from the chemical capacitance increases for the samples that underwent wet outdoor degradation, suggesting a higher degree of disorder of the blend under those conditions.

In addition, physical modeling and numerical simulations were carried out to support the conclusions obtained from the experiments. The simulations support the existence of an interfacial damaged layer near the anode contact with a worsened mobility. Moreover, good fits of the model to experimental $J-V$ curves under illumination for the degraded samples were obtained only when the model takes into account both a decreased mobility in a ∼120 nm layer and a reduced anode WF, confirming a worsening in charge extraction. Finally, simulations reveal a nonzero electric field across the active layer, indicating that these cells behave as p−i−n devices with an accumulation of majority carriers near the contacts. Furthermore, ideality factors obtained from simulations are in good agreement with experimental values of $n \sim 1$ after degradation, reinforcing the enhanced dominant SRH recombination near the anode.

■ ASSOCIATED CONTENT

Ⓢ Supporting Information

The Supporting Information is available free of charge at https://pubs.acs.org/doi/10.1021/acsaem.0c00711.

Device performance; AFM images; degradation characterization details; device physical modeling; and additional information on numerical simulations (PDF)

■ AUTHOR INFORMATION

Corresponding Author

Belén Arredondo − Área de Tecnología Electrónica, DELFO, Universidad Rey Juan Carlos, 28933 Móstoles, Spain; ⓞ orcid.org/0000-0002-9923-1225; Email: belen.arredondo@urjc.es

Authors

Gonzalo del Pozo − Área de Tecnología Electrónica, DELFO, Universidad Rey Juan Carlos, 28933 Móstoles, Spain

Enrique Hernández-Balaguera − Area de Tecnología Electrónica, DELFO, Universidad Rey Juan Carlos, 28933 Móstoles, Spain; ⓞ orcid.org/0000-0002-1400-5916

Diego Martín Martín − Área de Tecnología Electrónica, DELFO, Universidad Rey Juan Carlos, 28933 Móstoles, Spain

María del Carmen López González − Área de Tecnología Electrónica, DELFO, Universidad Rey Juan Carlos, 28933 Móstoles, Spain

Beatriz Romero − Área de Tecnología Electrónica, DELFO, Universidad Rey Juan Carlos, 28933 Móstoles, Spain

Eduardo López-Fraguas − Departamento de Tecnología Electrónica, GDAF-UC3M, Universidad Carlos III de Madrid, 28911 Leganés, Spain; ⓞ orcid.org/0000-0002-7943-4471

Ricardo Vergaz − Departamento de Tecnología Electrónica, GDAF-UC3M, Universidad Carlos III de Madrid, 28911 Leganés, Spain

Xabier Quintana − Departamento de Tecnología Fotónica y Bioingenieria, CEMDATIC, Universidad Politécnica de Madrid, 28040 Madrid, Spain

Jani Lamminaho − SDU NanoSYD, Mads Clausen Institute, University of Southern Denmark, 6400 Sønderborg, Denmark

Elodie Destouesse − SDU NanoSYD, Mads Clausen Institute, University of Southern Denmark, 6400 Sønderborg, Denmark

Mehrad Ahmadpour − SDU NanoSYD, Mads Clausen Institute, University of Southern Denmark, 6400 Sønderborg, Denmark; ⓞ orcid.org/0000-0001-9722-4163

Vida Turkovic − SDU NanoSYD, Mads Clausen Institute, University of Southern Denmark, 6400 Sønderborg, Denmark

Morten Madsen − SDU NanoSYD, Mads Clausen Institute, University of Southern Denmark, 6400 Sønderborg, Denmark; ⓞ orcid.org/0000-0001-6503-0479

Complete contact information is available at:
https://pubs.acs.org/10.1021/acsaem.0c00711

Author Contributions

All authors contributed to the manuscript and were involved in the discussion of results. J.L., E.D., V.T., and M.M. manufactured the devices. D.M.M. performed the physical simulations. The rest of the authors performed all of the characterization and circuital modeling. B.A. wrote the manuscript with contributions from E.H.-B., V.T., and M.M. All authors have given approval to the final version of the manuscript.

Notes

The authors declare no competing financial interest.

■ ABBREVIATIONS

BHJ, bulk heterojunction
CPE, constant phase element
DOS, density of states
EQE, external quantum efficiency
FF, fill factor
HUMO, highest unoccupied molecular orbital
IDL, internal damaged layer
IS, impedance spectroscopy
LUMO, lowest unoccupied molecular orbital
NFA, nonfullerene acceptor
OPV, organic photovoltaic
OSC, organic solar cell

686 PCE, power conversion efficiency
687 R2R, roll to roll
688 SRH, Shockley−Read−Hall
689 WF, work function

■ REFERENCES

691 (1) Ganesamoorthy, R.; Sathiyan, G.; Sakthivel, P. Review: Fullerene
692 Based Acceptors for Efficient Bulk Heterojunction Organic Solar Cell
693 Applications. *Sol. Energy Mater. Sol. Cells* **2017**, *161*, 102−148.
694 (2) Chen, J.-D.; Cui, C.; Li, Y.-Q.; Zhou, L.; Ou, Q.-D.; Li, C.; Li, Y.;
695 Tang, J.-X. Single-Junction Polymer Solar Cells Exceeding 10% Power
696 Conversion Efficiency. *Adv. Mater.* **2015**, *27*, 1035−1041.
697 (3) Liu, C.; Yi, C.; Wang, K.; Yang, Y.; Bhatta, R. S.; Tsige, M.; Xiao,
698 S.; Gong, X. Single-Junction Polymer Solar Cells with over 10%
699 Efficiency by a Novel Two-Dimensional Donor-Acceptor Conjugated
700 Copolymer. *ACS Appl. Mater. Interfaces* **2015**, *7*, 4928−4935.
701 (4) Liao, S.-H.; Jhuo, H.-J.; Yeh, P.-N.; Cheng, Y.-S.; Li, Y.-L.; Lee,
702 Y.-H.; Sharma, S.; Chen, S.-A. Single Junction Inverted Polymer Solar
703 Cell Reaching Power Conversion Efficiency 10.31% by Employing
704 Dual-Doped Zinc Oxide Nano-Film as Cathode Interlayer. *Sci. Rep.*
705 **2014**, *4*, No. 6813.
706 (5) Arredondo, B.; Romero, B.; Beliatis, M. J.; del Pozo, G.; Martín-
707 Martín, D.; Blakesley, J. C.; Dibb, G.; Krebs, F. C.; Gevorgyan, S. A.;
708 Castro, F. A. Analysing Impact of Oxygen and Water Exposure on
709 Roll-Coated Organic Solar Cell Performance Using Impedance
710 Spectroscopy. *Sol. Energy Mater. Sol. Cells* **2018**, *176*, 397−404.
711 (6) Gupta, S. K.; Pali, L. S.; Garg, A. Impedance Spectroscopy on
712 Degradation Analysis of Polymer/Fullerene Solar Cells. *Sol. Energy*
713 **2019**, *178*, 133−141.
714 (7) Sherafatipour, G.; Benduhn, J.; Patil, B. R.; Ahmadpour, M.;
715 Spoltore, D.; Rubahn, H.-G.; Vandewal, K.; Madsen, M. Degradation
716 Pathways in Standard and Inverted DBP-C 70 Based Organic Solar
717 Cells. *Sci. Rep.* **2019**, *9*, No. 4024.
718 (8) Wang, Y.; Jafari, M. J.; Wang, N.; Qian, D.; Zhang, F.; Ederth,
719 T.; Moons, E.; Wang, J.; Inganäs, O.; Huang, W.; Gao, F. Light-
720 Induced Degradation of Fullerenes in Organic Solar Cells: A Case
721 Study on TQ1:PC71BM. *J. Mater. Chem. A* **2018**, *6*, 11884−11889.
722 (9) Andreasen, B.; Tanenbaum, D. M.; Hermenau, M.; Voroshazi,
723 E.; Lloyd, M. T.; Galagan, Y.; Zimmernann, B.; Kudret, S.; Maes, W.;
724 Lutsen, L.; Vanderzande, D.; Würfel, U.; Andriessen, R.; Rösch, R.;
725 Hoppe, H.; Teran-Escobar, G.; Lira-Cantu, M.; Rivaton, A.;
726 Uzunoğlu, G. Y.; Germack, D. S.; Hösel, M.; Dam, H. F.;
727 Jørgensen, M.; Gevorgyan, S. A.; Madsen, M. V.; Bundgaard, E.;
728 Krebs, F. C.; Norrman, K. TOF-SIMS Investigation of Degradation
729 Pathways Occurring in a Variety of Organic Photovoltaic Devices–the
730 ISOS-3 Inter-Laboratory Collaboration. *Phys. Chem. Chem. Phys.*
731 **2012**, *14*, 11780−11799.
732 (10) Rösch, R.; Tanenbaum, D. M.; Jørgensen, M.; Seeland, M.;
733 Bärenklau, M.; Hermenau, M.; Voroshazi, E.; Lloyd, M. T.; Galagan,
734 Y.; Zimmermann, B.; Würfel, U.; Hösel, M.; Dam, H. F.; Gevorgyan,
735 S. A.; Kudret, S.; Maes, W.; Lutsen, L.; Vanderzande, D.; Andriessen,
736 R.; Teran-Escobar, G.; Lira-Cantu, M.; Rivaton, A.; Uzunoğlu, G. Y.;
737 Germack, D.; Andreasen, B.; Madsen, M. V.; Norrman, K.; Hoppe,
738 H.; Krebs, F. C. Investigation of the Degradation Mechanisms of a
739 Variety of Organic Photovoltaic Devices by Combination of Imaging
740 Techniques—the ISOS-3 Inter-Laboratory Collaboration. *Energy*
741 *Environ. Sci.* **2012**, *5*, 6521−6540.
742 (11) Tanenbaum, D. M.; Hermenau, M.; Voroshazi, E.; Lloyd, M.
743 T.; Galagan, Y.; Zimmermann, B.; Hösel, M.; Dam, H. F.; Jørgensen,
744 M.; Gevorgyan, S. A.; Kudret, S.; Maes, W.; Lutsen, L.; Vanderzande,
745 D.; Würfel, U.; Andriessen, R.; Rösch, R.; Hoppe, H.; Teran-Escobar,
746 G.; Lira-Cantu, M.; Rivaton, A.; Uzunoğlu, G. Y.; Germack, D.;
747 Andreasen, B.; Madsen, M. V.; Norrman, K.; Krebs, F. C. The ISOS-3
748 Inter-Laboratory Collaboration Focused on the Stability of a Variety
749 of Organic Photovoltaic Devices. *RSC Adv.* **2012**, *2*, 882−893.
750 (12) Turkovic, V.; Engmann, S.; Tsierkezos, N.; Hoppe, H.; Madsen,
751 M.; Rubahn, H.-G.; Ritter, U.; Gobsch, G. Long-Term Stabilization of

752 Organic Solar Cells Using Hydroperoxide Decomposers as Additives.
753 *Appl. Phys. A: Mater. Sci. Process.* **2016**, *122*, No. 255.
754 (13) Turkovic, V.; Prete, M.; Bregnhøj, M.; Inasaridze, L.; Volyniuk,
755 D.; Obrezkov, F. A.; Grazulevicius, J. V.; Engmann, S.; Rubahn, H.-G.;
756 Troshin, P. A.; Ogilby, P. R.; Madsen, M. Biomimetic Approach to
757 Inhibition of Photooxidation in Organic Solar Cells Using Beta-
758 Carotene as an Additive. *ACS Appl. Mater. Interfaces* **2019**, *11*,
759 41570−41579.
760 (14) Zhao, W.; Qian, D.; Zhang, S.; Li, S.; Inganäs, O.; Gao, F.;
761 Hou, J. Fullerene-Free Polymer Solar Cells with over 11% Efficiency
762 and Excellent Thermal Stability. *Adv. Mater.* **2016**, *28*, 4734−4739.
763 (15) Upama, M. B.; Wright, M.; Mahmud, M. A.; Elumalai, N. K.;
764 Soufiani, A. M.; Wang, D.; Xu, C.; Uddin, A. Photo-Degradation of
765 High Efficiency Fullerene-Free Polymer Solar Cells. *Nanoscale* **2017**,
766 *9*, 18788−18797.
767 (16) An, Q.; Zhang, F.; Gao, W.; Sun, Q.; Zhang, M.; Yang, C.;
768 Zhang, J. High-Efficiency and Air Stable Fullerene-Free Ternary
769 Organic Solar Cells. *Nano Energy* **2018**, *45*, 177−183.
770 (17) Li, S.; Ye, L.; Zhao, W.; Zhang, S.; Mukherjee, S.; Ade, H.;
771 Hou, J. Energy-Level Modulation of Small-Molecule Electron
772 Acceptors to Achieve over 12% Efficiency in Polymer Solar Cells.
773 *Adv. Mater.* **2016**, *28*, 9423−9429.
774 (18) Li, S.; Ye, L.; Zhao, W.; Yan, H.; Yang, B.; Liu, D.; Li, W.; Ade,
775 H.; Hou, J. A Wide Band Gap Polymer with a Deep Highest
776 Occupied Molecular Orbital Level Enables 14.2% Efficiency in
777 Polymer Solar Cells. *J. Am. Chem. Soc.* **2018**, *140*, 7159−7167.
778 (19) Speller, E. M.; Clarke, A. J.; Aristidou, N.; Wyatt, M. F.;
779 Francàs, L.; Fish, G.; Cha, H.; Lee, H. K. H.; Luke, J.; Wadsworth, A.;
780 Evans, A. D.; McCulloch, I.; Kim, J.-S.; Haque, S. A.; Durrant, J. R.;
781 Dimitrov, S. D.; Tsoi, W. C.; Li, Z. Toward Improved Environmental
782 Stability of Polymer:Fullerene and Polymer:Nonfullerene Organic
783 Solar Cells: A Common Energetic Origin of Light- and Oxygen-
784 Induced Degradation. *ACS Energy Lett.* **2019**, *4*, 846−852.
785 (20) Yan, C.; Barlow, S.; Wang, Z.; Yan, H.; Jen, A. K.-Y.; Marder, S.
786 R.; Zhan, X. Non-Fullerene Acceptors for Organic Solar Cells. *Nat.*
787 *Rev. Mater.* **2018**, *3*, No. 18003.
788 (21) Cui, Y.; Yao, H.; Zhang, J.; Zhang, T.; Wang, Y.; Hong, L.;
789 Xian, K.; Xu, B.; Zhang, S.; Peng, J.; Wei, Z.; Gao, F.; Hou, J. Over
790 16% Efficiency Organic Photovoltaic Cells Enabled by a Chlorinated
791 Acceptor with Increased Open-Circuit Voltages. *Nat. Commun.* **2019**,
792 *10*, No. 2515.
793 (22) Fan, B.; Zhang, D.; Li, M.; Zhong, W.; Zeng, Z.; Ying, L.;
794 Huang, F.; Cao, Y. Achieving over 16% Efficiency for Single-Junction
795 Organic Solar Cells. *Sci. China Chem.* **2019**, *62*, 746−752.
796 (23) Zhang, S.; Qin, Y.; Zhu, J.; Hou, J. Over 14% Efficiency in
797 Polymer Solar Cells Enabled by a Chlorinated Polymer Donor. *Adv.*
798 *Mater.* **2018**, *30*, No. 1800868.
799 (24) Zheng, Z.; Hu, Q.; Zhang, S.; Zhang, D.; Wang, J.; Xie, S.;
800 Wang, R.; Qin, Y.; Li, W.; Hong, L.; Liang, N.; Liu, F.; Zhang, Y.;
801 Wei, Z.; Tang, Z.; Russell, T. P.; Hou, J.; Zhou, H. A Highly Efficient
802 Non-Fullerene Organic Solar Cell with a Fill Factor over 0.80 Enabled
803 by a Fine-Tuned Hole-Transporting Layer. *Adv. Mater.* **2018**, *30*,
804 No. 1801801.
805 (25) Baran, D.; Kirchartz, T.; Wheeler, S.; Dimitrov, S.; Abdelsamie,
806 M.; Gorman, J.; Ashraf, R. S.; Holliday, S.; Wadsworth, A.; Gasparini,
807 N.; Kaienburg, P.; Yan, H.; Amassian, A.; Brabec, C. J.; Durrant, J. R.;
808 McCulloch, I. Reduced Voltage Losses Yield 10% Efficient Fullerene
809 Free Organic Solar Cells with > 1 V Open Circuit Voltages. *Energy*
810 *Environ. Sci.* **2016**, *9*, 3783−3793.
811 (26) Qian, D.; Zheng, Z.; Yao, H.; Tress, W.; Hopper, T. R.; Chen,
812 S.; Li, S.; Liu, J.; Chen, S.; Zhang, J.; Liu, X.-K.; Gao, B.; Ouyang, L.;
813 Jin, Y.; Pozina, G.; Buyanova, I. A.; Chen, W. M.; Inganäs, O.;
814 Coropceanu, V.; Bredas, J.-L.; Yan, H.; Hou, J.; Zhang, F.; Bakulin, A.
815 A.; Gao, F. Design Rules for Minimizing Voltage Losses in High-
816 Efficiency Organic Solar Cells. *Nat. Mater.* **2018**, *17*, 703.
817 (27) Holliday, S.; Ashraf, R. S.; Wadsworth, A.; Baran, D.; Yousaf, S.
818 A.; Nielsen, C. B.; Tan, C.-H.; Dimitrov, S. D.; Shang, Z.; Gasparini,
819 N.; Alamoudi, M.; Laquai, F.; Brabec, C. J.; Salleo, A.; Durrant, J. R.;
820 McCulloch, I. High-Efficiency and Air-Stable P3HT-Based Polymer

Solar Cells with a New Non-Fullerene Acceptor. *Nat. Commun.* **2016**, 7, No. 11585.

(28) Lin, Y.; Zhao, F.; He, Q.; Huo, L.; Wu, Y.; Parker, T. C.; Ma, W.; Sun, Y.; Wang, C.; Zhu, D.; Heeger, A. J.; Marder, S. R.; Zhan, X. High-Performance Electron Acceptor with Thienyl Side Chains for Organic Photovoltaics. *J. Am. Chem. Soc.* **2016**, *138*, 4955−4961.

(29) Doumon, N. Y.; Dryzhov, M. V.; Houard, F. V.; Le Corre, V. M.; Rahimi Chatri, A.; Christodoulis, P.; Koster, L. J. A. Photostability of Fullerene and Non-Fullerene Polymer Solar Cells: The Role of the Acceptor. *ACS Appl. Mater. Interfaces* **2019**, *11*, 8310−8318.

(30) Du, X.; Heumueller, T.; Gruber, W.; Classen, A.; Unruh, T.; Li, N.; Brabec, C. J. Efficient Polymer Solar Cells Based on Non-Fullerene Acceptors with Potential Device Lifetime Approaching 10 Years. *Joule* **2019**, *3*, 215−226.

(31) Luke, J.; Speller, E. M.; Wadsworth, A.; Wyatt, M. F.; Dimitrov, S.; Lee, H. K. H.; Li, Z.; Tsoi, W. C.; McCulloch, I.; Bagnis, D.; Durrant, J. R.; Kim, J.-S. Twist and Degrade—Impact of Molecular Structure on the Photostability of Nonfullerene Acceptors and Their Photovoltaic Blends. *Adv. Energy Mater.* **2019**, *9*, No. 1803755.

(32) Destouesse, E.; Top, M.; Lamminaho, J.; Rubahn, H.-G.; Fahlteich, J.; Madsen, M. Slot-Die Processing and Encapsulation of Non-Fullerene Based ITO-Free Organic Solar Cells and Modules. *Flexible Printed Electron.* **2019**, *4*, No. 045004.

(33) Reese, M. O.; Gevorgyan, S. A.; Jørgensen, M.; Bundgaard, E.; Kurtz, S. R.; Ginley, D. S.; Olson, D. C.; Lloyd, M. T.; Morvillo, P.; Katz, E. A.; Elschner, A.; Haillant, O.; Currier, T. R.; Shrotriya, V.; Hermenau, M.; Riede, M.; R. Kirov, K.; Trimmel, G.; Rath, T.; Inganäs, O.; Zhang, F.; Andersson, M.; Tvingstedt, K.; Lira-Cantu, M.; Laird, D.; McGuiness, C.; Gowrisanker, S.; Pannone, M.; Xiao, M.; Hauch, J.; Steim, R.; DeLongchamp, D. M.; Rösch, R.; Hoppe, H.; Espinosa, N.; Urbina, A.; Yaman-Uzunoglu, G.; Bonekamp, J.-B.; van Breemen, A. J. J. M.; Girotto, C.; Voroshazi, E.; Krebs, F. C. Consensus Stability Testing Protocols for Organic Photovoltaic Materials and Devices. *Sol. Energy Mater. Sol. Cells* **2011**, *95*, 1253−1267.

(34) López-Fraguas, E.; Sánchez-Pena, J. M.; Vergaz, R. A Low-Cost LED-Based Solar Simulator. *IEEE Trans. Instrum. Meas.* **2019**, *68*, 4913.

(35) Yao, H.; Cui, Y.; Yu, R.; Gao, B.; Zhang, H.; Hou, J. Design, Synthesis, and Photovoltaic Characterization of a Small Molecular Acceptor with an Ultra-Narrow Band Gap. *Angew. Chem., Int. Ed.* **2017**, *56*, 3045−3049.

(36) Wang, T.-L.; Yang, C.-H.; Chuang, Y.-Y. A Comparative Study of the Effect of Fluorine Substitution on the Photovoltaic Performance of Benzothiadiazole-Based Copolymers. *RSC Adv.* **2016**, *6*, 47676−47686.

(37) Jørgensen, M.; Norrman, K.; Gevorgyan, S. A.; Tromholt, T.; Andreasen, B.; Krebs, F. C. Stability of Polymer Solar Cells. *Adv. Mater.* **2012**, *24*, 580−612.

(38) Xu, T.; Gong, C.; Wang, S.; Lian, H.; Lan, W.; Lévêque, G.; Grandidier, B.; Plain, J.; Bachelot, R.; Wei, B.; Zhu, F. Ultraviolet-Durable Flexible Nonfullerene Organic Solar Cells Realized by a Hybrid Nanostructured Transparent Electrode. *Sol. RRL* **2020**, *4*, No. 1900522.

(39) Tress, W.; Yavari, M.; Domanski, K.; Yadav, P.; Niesen, B.; Baena, J. P. C.; Hagfeldt, A.; Graetzel, M. Interpretation and Evolution of Open-Circuit Voltage, Recombination, Ideality Factor and Subgap Defect States during Reversible Light-Soaking and Irreversible Degradation of Perovskite Solar Cells. *Energy Environ. Sci.* **2018**, *11*, 151−165.

(40) Wang, Y.; Lan, W.; Li, N.; Lan, Z.; Li, Z.; Jia, J.; Zhu, F. Stability of Nonfullerene Organic Solar Cells: From Built-in Potential and Interfacial Passivation Perspectives. *Adv. Energy Mater.* **2019**, *9*, No. 1900157.

(41) Qi, B.; Wang, J. Fill Factor in Organic Solar Cells. *Phys. Chem. Chem. Phys.* **2013**, *15*, 8972−8982.

(42) Hirschorn, B.; Orazem, M. E.; Tribollet, B.; Vivier, V.; Frateur, I.; Musiani, M. Determination of Effective Capacitance and Film Thickness from Constant-Phase-Element Parameters. *Electrochim. Acta* **2010**, *55*, 6218−6227.

(43) Bässler, H. Charge Transport in Disordered Organic Photoconductors a Monte Carlo Simulation Study. *Phys. Status Solidi B* **1993**, *175*, 15−56.

(44) Turcu, M.; Pakma, O.; Rau, U. Interdependence of absorber composition and recombination mechanism in Cu(In,Ga)(Se,S)2 heterojunction solar cells. *Appl. Phys. Lett.* **2019**, *80*, 2598.